ARTICLE

Luminescent and magnetic [TbEu] 2D Metal-Organic Frameworks

E. Bartolomé[a*], A. Arauzo[b], S. Fuertes[c], L. Navarro-Spreafica[d], P. Sevilla[a], H. Fernández Cortés,[d] N. Settineri,[e] S. J. Teat,[e] E. C. Sañudo[d,f*]

We present the synthesis, through a simple, microwave-assisted method, of lanthanoid-based 2D metal-organic frameworks (MOFs) of general formula [$Ln_xLn'_{1-x}$(MeCOO)(PhCOO)$_2$], including homonuclear compounds (x=1), Ln=Eu, Tb, and heterometallic compounds, [TbEu]. The crystalline material is formed by neutral nanosheets held together by Van der Waals interactions, which can be easily exfoliated by sonication. Photoluminescent emission in the visible range was observed for all the synthesized 2D MOF compounds via excitation of the ligand, showing benzoates are efficient antenna ligands. Efficient energy transfer from Tb→Eu was observed in the heterometallic [TbEu] compounds, which could potentially perform as luminescent thermometers. Inks containing nanosheets of 2D MOFs exfoliated in solution were prepared, and luminescent prints of Tb and Eu 2D MOFs on paper were made to show the possible application for anticounterfeiting. Frequency-dependent ac susceptibility results show the occurrence of slow magnetic relaxation in [TbEu] compounds through direct relaxation mechanisms, affected by bottleneck effect. A slowing down of the relaxation time is observed as the Eu/Tb ratio increases.

1. Introduction

Molecular systems including lanthanoid ions constitute a very active research area within material science due to their exceptional physical properties, which make them attractive for numerous applications, such as optical and magnetic resonance imaging,[1,2] magnetic refrigeration,[3,4] light-emitting diodes,[5,6] information storage and processing,[7,8] quantum technology and sensors etc.

In view of this potential, important efforts have been done towards developing molecular systems with more than one type of lanthanoid ion. Combinations of different lanthanoids can be used to improve up-conversion[9] efficiency in luminescent systems, modify the color or brightness of their emission,[10,11] for anticounterfeiting,[12] to produce contrast agents covering both visible and near-IR regions,[13] for thermometric probes[14,15] etc. In the field of information processing[16], heterometallic [LnLn'] dinuclear complexes have been proposed for the realization of two quantum bits (qubits) quantum gates (qugates) for quantum computing[16–18] and spin valves,[19] whereas trinuclear [LnLn'Ln][20] complexes can be used to perform quantum error correction protocols[21] or three qubit qugates.

The electronic properties of Ln(III) make them ideal for the design of both luminescent materials[22–25] and Single-Molecule Magnets (SMMs).[8,26,27] On the one hand Ln(III)-based complexes deploy intense, narrow-banded, long-lived emission bands covering the visible and near-infrared spectrum, although luminescence must be usually sensitized through an "antenna" ligand, given that direct excitation of the Ln ions rarely provides high emission yields. On the other hand, the unquenched orbital moment of some Ln(III), confers them with high magnetic anisotropy which favors slow relaxation of the magnetization.[8] Lanthanoid-based Single-Ion Magnets (SIMs) with activation energies of ca. 2000 K operating at temperatures above liquid nitrogen[28] have been recently achieved, thanks to adequate tailoring of the Ln(III) coordination environment and symmetry. Interestingly, heterometallic Ln-Ln' lanthanoid complexes have more potential to incorporate multifunctionality, i.e.

luminescent and magnetic properties by judicious choice of the metal centers.[11]

However, the goal of preparing heterometallic Ln-Ln' molecular compounds remains challenging, given that all the metals of the lanthanoid series are very similar. Some of the approaches adopted for the preparation of mixed lanthanoid compounds lead to a statistical distribution of the Ln/Ln' ions in the crystal,[10,11] which is sufficient for certain applications. For others, such as qubits, a selective distribution of the different Ln ions in the molecular entity is needed. Thus, different synthetic procedures have been developed to achieve mixed compounds where Ln/Ln' ions stay in selected sites: i) by step-by-step procedure[29–32] ii) by linking pre-formed metal-containing moieties;[33,34] or iii) during the course of one-pot reactions, by using ligands with two types of coordination pockets that are able to discriminate different Ln's by their radius.[35–37] The synthetic procedures reported up to date have allowed synthesizing heterometallic lanthanoid compounds of different dimensionality: dinuclear [Ln'Ln][29–31,35,36,38,39] and trinuclear [LnLn'Ln][32,37] entities; macrocycles[30], 1D polymeric chains[40], 2D coordination polymers[14,41] and 3D MOFs.[15,42–44]

On the other hand, two-dimensional materials are receiving growing attention nowadays, and the synthesis of 2D metal-organic frameworks (2D MOFs)[45–47] through coordination chemistry represents a flexible, versatile alternative to inorganic solids[48]. The large horizontal and ultra-thin dimensions of 2D MOFs lead to very high values of specific surface, atomic surface ratio and number of active places exposed to surface, which can enhance some capabilities as compared to bulk materials.[49,50] For 2D MOFs formed of neutral nanosheets separated by Van der Waal forces, exfoliation in solution can be used to produce nanosheets that are stable towards aggregation.[51–53] Furthermore, luminescent lanthanoid-based MOFs in suspension have been recently used for smart sensing of methylmalonic acid and anticounterfeiting applications.[54]

In two recent papers, we presented a facile, microwave-assisted method for the synthesis of a Dy and Tb carboxylate-based 2D MOFs

formed by neutral nanosheets held together by Van der Waals interactions. The material was easily exfoliated into nanosheets by sonication in solution,[55] opening the possibility of depositing the 2D material on a surface[56] or exploiting it in heterostructures. Herein, the same synthetic method was used to prepare isostructural heterometallic [TbEu] 2D MOFs of general formula [$Tb_xEu_{1-x}(MeCOO)(PhCOO)_2$] of various compositions. We report and discuss here the luminescent and magnetic properties of [Tb_xEu_{1-x}] 2D MOFs as a function of the x=Tb/Eu ratio.

2. Experimental

Synthesis. All chemicals and solvents were purchased from commercial sources and used as received.

Tb and **Eu** [$Ln(MeCOO)(PhCOO)_2$]: the synthesis of homonuclear compound, with Ln=Eu was based on the procedure previously described for Ln=Dy (CCDC-2017957)[55] and Ln=Tb (CCDC-2095560)[56] compounds. **Eu:** [$Eu(MeCOO)(PhCOO)_2$]·$(H_2O)_{0.25}$] C 41.88 (41.87)% H 2.97 (2.86)% N 0 (0)%.

TbEu [$Tb_xEu_{1-x}(MeCOO)(PhCOO)_2$]: a total of 0.26 mmol of hydrated $Tb(MeCOO)_3$·(0.26 - x mmol) and $Eu(MeCOO)_3$ (x mmol) in the desired ratios and 0.063 g of PhCOOH (0.52 mmol) were placed in a CEM Discover Microwave Reactor with 4 mL of a MeOH:MeCN 1:1 mixture. A pulse of 150 W was applied and the reaction kept for 10 minutes at a maximum temperature of 125ºC. The reaction was cooled to room temperature and a colorless precipitate was filtered off. The solution was left for 9 days at 40ºC; after this time colorless crystals of the 2D MOFs were obtained. All yields are between 50% and 80%. Tb/Eu ratio in the heternuclear samples was determined by ICP analysis. Elemental analyses as calculated (experimental): **$Tb_{0.2}Eu_{0.8}$**: [$Tb_{0.17}Eu_{0.83}(MeCOO)(PhCOO)_2$]·$(H_2O)$ C 41.50 (41.20) % H 3.01 (2.97) % N 0 (0)%; **$Tb_{0.3}Eu_{0.7}$**: [$Tb_{0.28}Eu_{0.72}(MeCOO)(PhCOO)_2$]·$(CH_3CN)_{0.14}(H_2O)_{0.61}$ C 41.31 (41.02) % H 3.12 (2.83) % N 0.41 (0.71) %; **$Tb_{0.4}Eu_{0.6}$.** [$Tb_{0.42}Eu_{0.58}(CH_3COO)(PhCOO)_2$] (%): C: 42.00, H: 2.87, N: 0; **$Tb_{0.7}Eu_{0.3}$:** [$Tb_{0.71}Eu_{0.29}(CH_3COO)(PhCOO)_2(H_2O)_{0.5}$]: C 41.04 (40.84) % H 3.02 (2.86) % N 0 (0) %; **$Tb_{0.9}Eu_{0.1}$:** [$Tb_{0.86}Eu_{0.14}(CH_3COO)(PhCOO)_2(H_2O)_{0.5}$]: C 41.03(40.81) % H 3.01(2.77) % N 0(0) %.

Exfoliation. Exfoliation of 2D MOF bulk compounds into stable nanosheets was carried out by sonication. Samples presented here were prepared following several procedures: (1) 1 mg of microcrystals in 10 mL of i-propanol were sonicated at 30°C for 1h or (2) 30'; (3) 5 mg of microcrystals were sonicated in 5 mL of i-propanol for 30' and centrifuged twice: firstly, for one minute at 2000 rpm and decanted to eliminate big crystals, and finally centrifuged again for another minute at 6000 rpm and decanted to eliminate smaller microcrystals. The sonicator used was an Ultrasonic Cleaner VWR and the centrifuge an EBA 21 Hettich Zentrifugen machine. The presence of nanosheets in all obtained suspensions was demonstrated by the Tyndall effect.

TEM-EDX and SEM-EDS. Scanning Electron Microscopy (JEOL 2100) and Transmission Electron Microscopy (JEM 2100) were done in the

Centres Científics i Tecnològics of the University of Barcelona (CCiTUB). The microscopes have an integrated Energy Dispersed X-ray Detector for elemental analysis.

X-Ray Diffraction. Single crystal X-ray diffraction data for **Eu** and **TbEu** were collected with a Bruker APEXII SMART diffractometer using Molybdenum K-alfa microfocus radiation source (lambda= 0.71073 Å) at GMMF, only a unit cell was obtained. Samples were taken to synchrotron source 'Advanced Light Source, beamline 12.2.1 (Berkeley, USA) and collected using shutterless phi and omega scans on a Bruker D8 with PHOTON II detector at 0.7288 nm. The structures were solved by Patterson or intrinsic phasing methods (SHELXS2013 and SHELXT) and refined on F2(SHELXL-2016). Hydrogen atoms were included on calculated positions, riding on their carrier atoms. The Tb:Eu ratio for TbEu was fixed to solve the crystal structure. The value was obtained from the relevant characterization done for the compound and discussed in this work. Cif files of **Eu** (CCDC-2169279) and **$Tb_{0.4}Eu_{0.6}$** (CCDC- 2169280) can be obtained free of charge from the Cambridge Structural Database (http://www.ccdc.cam.ac.uk/). PXRD was done at CCCiTUB with a PANalytical X'Pert PRO MPD θ/θ powder diffractometer with Cu K_α radiation (λ = 1.5418 Å). Samples were sandwiched between films of polyester of 3,6 microns of thickness

Inductively coupled plasma spectrometry and fluorescence analyses. The Tb^{3+}/Eu^{3+} ion ratio of all TbEu samples was determined by inductively coupled plasma optical emission spectrometry (ICP-OES), using a Thermo Scienfitic i-CAP PRO XP Duo Spectrometer. In addition, fluorescence analysis of samples **$Tb_{0.9}Eu_{0.1}$** and **$Tb_{0.7}Eu_{0.3}$** was performed using a Thermo Fisher sequential X-ray fluorescence spectrometer, ARL PERFOM'X series, with a Rhodium (Rh) X-ray tube, and the UNIQUANT program was used for semiquantitative analysis without standards.

Infrared spectroscopy. ATR-IR spectroscopy has been done in the University of Barcelona (UB), at the department of Inorganic and Organic Chemistry using a spectrophotometer FT-IR Nicolet iS5.

Solid state and solution luminescent measurements. Quantum yields (QY) were measured under excitation wavelengths ranging from λ_{exc}=275-415 nm at 300 K using a Hamamatsu Absolute PL Quantum Yield spectrometer C11347 (Hamamatsu Quantaurus QY). The absolute QY (ratio of the number of photons emitted by photoluminescence to the number of photons absorbed by the light-emitting material) was measured using an integrating sphere. Powdered samples were placed in a capillary with an internal diameter of 4 mm. Solution samples were placed in a standard quartz cell. The absorption and emission spectra of the sample container (the blank) were separately recorded. The QY was calculated as: $Q = (E_c - E_a)/(L_a - L_c)$, with E_c being the integrated emission Q_{Eu}^{lig} spectrum of the sample, E_a the integrated blank emission spectrum, L_a the blank[57] absorption, and L_c the sample absorption at the excitation wavelength.

ARTICLE
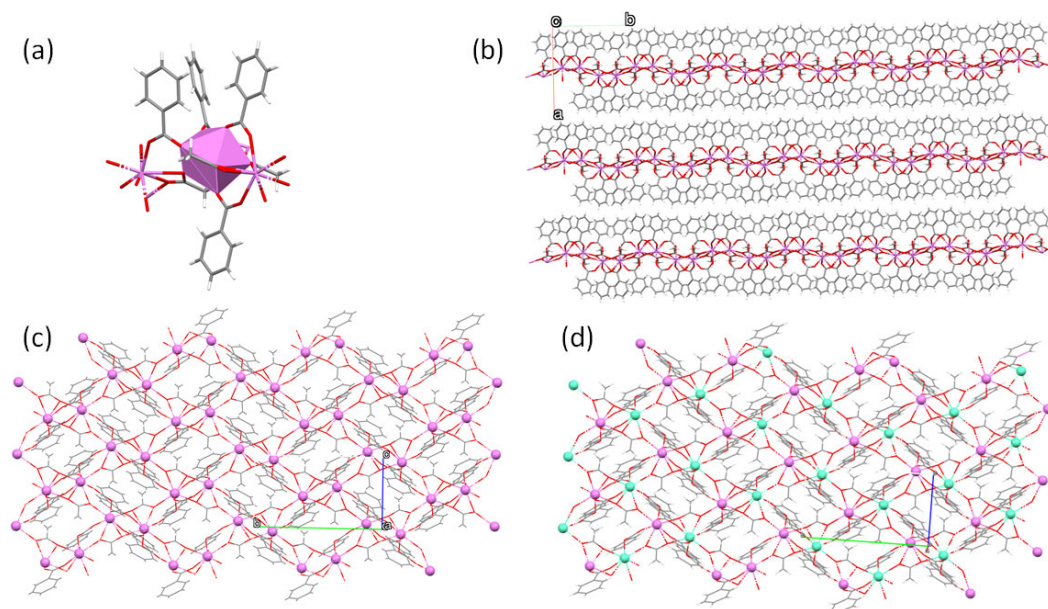
Figure 1. (a) Crystal structure of [Eu(MeCOO)(PhCOO)$_2$] **Eu**, with one Eu(III) ion in polyhedral representation; (b) Crystal packing of **Eu** along the *c*-xis of the unit cell showing three Van der Waals stacked nanosheets; (c) and (d) show one nanosheet viewed along *a*-axis of the unit cell for **Eu** (c) and **Tb$_{0.4}$Eu$_{0.6}$** (d). Carbon in grey, hydrogen in light grey, oxygen in red, europium in pink and terbium in green.
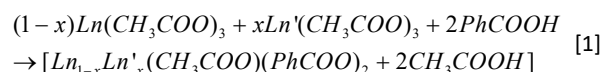
Photoluminescence emission and excitation spectra of **Tb**, **Eu** and **TbEu** samples were measured using a Fluorolog FL-1057 Jobin Ybon HORIBA spectrofluorometer at UZ. Phosphorescence lifetimes were recorded with a Fluoromax phosphorimeter accessory containing a UV xenon flash tube. Excitation spectra were recorded at the energy (λ_{mon}) at which the emission spectra presented the most intense peak for each lanthanoid. Lifetimes shorter than 10 µs were recorded with a Datastation HUB-B using a 340 nm nanoLED light source generating short optical pulses and associated acquisition electronics package DAS6. In addition, luminescence measurements of **Tb**, **Eu** exfoliated solutions on paper were performed using a spectro-fluorometer NanologTM-Horiba Jobyn Yvon at the UB.Emission spectra and lifetimes at LNT were performed by immersion of the sample quartz tube in a liquid-nitrogen-filled optical dewar.

Magnetometry. The magnetization, dc and ac susceptibility of powdered and exfoliated solution samples were measured, above 1.8 K, using a Quantum Design superconducting quantum interference device (SQUID) magnetometer. Ac measurements were done at an excitation field of 4 Oe, at temperatures between 1.8 K - 8.0 K, under dc fields between 0 - 30 kOe, while sweeping the frequency between 0.1 and 1000 Hz. Additional ac measurements in an extended frequency range, 10< *f*< 10 kHz, were performed in a Quantum Design PPMS ACMS magnetometer. Measurements on powdered samples were done with the addition of Daphne oil, introduced to fix the grains at low temperatures. Exfoliated samples in isopropanol solution were placed in a gelatin

capsule sealed with vacuum grease. The capsule was completely filled with the solution, with the help of a syringe, avoiding the formation of air bubbles to prevent oxygen contamination.

3. Synthesis and structural characterization

The homometallic **Eu** 2D MOF was prepared following the reported procedure for Tb and Dy analogues.[55,56] For heterometallic **TbEu** 2D MOFs, the synthesis is the same as for homometallic compounds, but mixing two different Ln(CH$_3$COO)$_3$ and Ln'(CH$_3$COO)$_3$ as shown in Eq. [1]:

$$(1-x)Ln(CH_3COO)_3 + xLn'(CH_3COO)_3 + 2PhCOOH$$
$$\rightarrow [Ln_{1-x}Ln'_x(CH_3COO)(PhCOO)_2 + 2CH_3COOH] \quad [1]$$

The IR spectra of the homometallic complex **Eu** is similar to the IR spectra reported for Dy and Tb analogues (Fig. S1) suggesting they all have the same ligands in the same binding modes.

The crystallographic and data collection parameters for **Eu** and **Tb$_{0.3}$Eu$_{0.7}$** are collected in Table 1. The two 2D MOFs are isostructural to **Dy** and **Tb** analogues previously reported by us. They crystallize in the monoclinic space group P2$_1$/m. Each Eu(III) and Tb(III) ion has a coordination number 8, with a distorted square antiprism coordination environment (Fig. 1a). The unit cell volumes of the homometallic and heterometallic complexes follow the expected pattern of size change due to the lanthanoid contraction. For the heterometallic complex, the average ionic radii is used for Eu/Tb.

ARTICLE   Journal Name

Table 1. Single crystal X-ray diffraction parameters for **Eu** and **Tb$_{0.3}$ Eu$_{0.7}$** 2D MOF compounds.		
Formula	[Eu(MeCOO)(PhCOO)$_2$] (**Eu**)	[Tb$_{0.3}$Eu$_{0.7}$(CH$_3$COO)(PhCOO)$_2$] (**Tb$_{0.28}$Eu$_{0.72}$**)
CSD	2169279	2169280
Crystal system	Monoclinic	Monoclinic
Space group	P2$_1$/c	P2$_1$/c
Z	4	4
a (Å)	16.3757(13)	16.3636(13)
b (Å)	12.7379(9)	12.6892(10)
c (Å)	7.2766(6)	7.2847(6)
α	90	90
β°	100.931(4)	101.030(3)
γ°	90	90
V (Å^3)	1490.3(2)	1484.7(2)
T (K)	100	100
Gof	1.095	1.073
R (wR)	0.0436 (0.1059)	0.0401 (0.1100)

The unit cell volume for **Tb$_{0.3}$Eu$_{0.7}$** has a value of 1484.7 Å^3, between the values of the volume for the unit cell of **Eu**, 1490.3 Å^3 reported here and of **Tb**, 1479.2 Å^3 reported elsewhere.[56]

This helps confirm that the **Tb$_{0.3}$Eu$_{0.7}$** analogue is indeed a crystal with statistically distributed Eu and Tb ions and not a mixture of Eu MOF and Tb MOF crystals.

The structure shows a Van der Waals stack of 2D nanosheets that contain acetato groups and lanthanoid ions within a corrugated layer and benzoato groups between the layers, as shown in Fig. 1b. Within the 2D layer, the Ln ions are arranged forming a distorted honeycomb (Fig. 1c). The crystals obtained for these species are colorless platelets and can be easily identified by SEM.

In order to characterize the homometallic and heterometallic **TbEu** of different compositions. Powder X-ray diffraction (PXRD) patterns were collected and compared to the calculated PXRD for **Eu**, **Tb** and **Tb$_{0.3}$Eu$_{0.7}$**. The IR spectra of all complexes were also collected. The IR spectra follow the same pattern and indicate the compounds share the same structure and coordination modes for the carboxylate ligands. Fig. 2a shows the experimental PXRD patterns for **Eu** and **Tb$_{0.2}$Eu$_{0.8}$** 2D MOFs and the calculated PXRD pattern for **Eu** 2D MOF and the heterometallic **Tb$_{0.3}$Eu$_{0.7}$** 2D MOF. All other PXRD patterns can be found in the supplementary material (Fig. S2). The PXRD patterns of heterometallic complexes confirm they are all isostructural to the homometallic **Eu**, **Tb** and **Dy** analogues.

The series of isostructural mixed 2D MOFs are denoted **TbEu**. In order to ascertain whether the molar amounts of Tb and Eu used in the synthesis were found in the crystals, elemental analysis and ICP measurements were performed (Fig. S3). The analysis of samples are within accepted error of the calculated values for the general formula [Ln$_{1-x}$Ln'$_x$(CH$_3$COO)(PhCOO)$_2$]. For the heterometallic cases, the relative amount of lanthanoid ions observed was slightly different to the expected from the Tb:Eu ratio used in the microwave assisted synthesis.

Figure 3 shows SEM images of **Eu**, **Tb** and selected heterometallic samples. All of them show the expected platelet crystals already reported for the Dy 2D MOF. The solubility of the compound depends on the nature of the lanthanoid ion, and less soluble complexes show poorly shaped crystals in SEM. The SEM images show the formation of regular platelet crystals, of micrometer sizes, with the shortest dimension being extremely small, of the order of 0.5-2 micrometers. EDS measurements performed on these samples yielded Tb/Eu ratios compatible the more accurate ratios determined by ICP (Fig. S3). For

the heterometallic complexes, we propose a statistical distribution of the Tb:Eu ions in the nanosheets, as that shown in Fig. 1d for **Tb$_{0.3}$Eu$_{0.7}$**.

In our previous report of the Dy analogue[55] the Van der Waals interactions between layers were calculated to be of the order of those in graphene. Thus, exfoliation of these materials into flakes and even individual nanosheets was demonstrated for Dy and later on for Tb.[56] In this work, we follow the same protocol to exfoliate or delaminate the homo and heterometallic 2D materials prepared here. This is a mild exfoliation method that relies on placing the crystals in isopropanol and applying ultrasounds in a laboratory ultrasound bath for 30 minutes to 1 hour. Colorless dispersions of flakes that display the Tyndall-Faraday effect are obtained for all samples. TEM microscopy of the dispersions confirm the presence of flakes and nanosheets, as shown in Figure 3. More TEM images and EDX analysis for **Tb$_{0.4}$Eu$_{0.6}$** are shown in ESI Figure .[55,56]
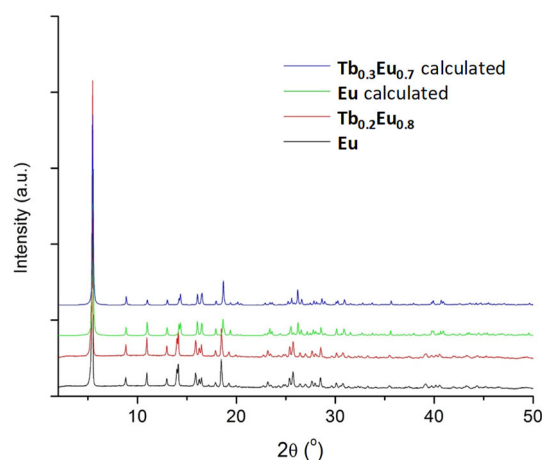
Figure 2. Calculated PXRD from single crystal data for **Eu** and **Tb$_{0.3}$Eu$_{0.7}$** and experimental PXRD plots for of **Eu** and **Tb$_{0.2}$Eu$_{0.8}$** 2D MOFs.
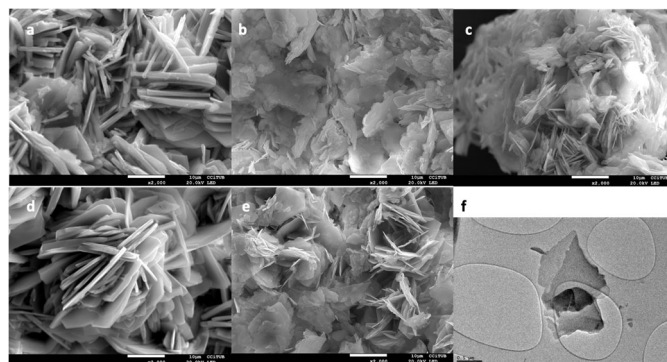
Figure 3. SEM images of (top) homometallic a) **Tb**, b) **Eu** and heterometallic 2D MOFs c) **Tb$_{0.2}$Eu$_{0.8}$**, d) **Tb$_{0.3}$Eu$_{0.7}$** and e) **Tb$_{0.4}$Eu$_{0.6}$**. The measuring bar is in all images 10 μm. f) TEM image of a flake of **Tb$_{0.4}$Eu$_{0.6}$**. The bar is 0.5 μm.

4. Luminescence results

All the studied 2D MOFs in bulk showed visible emission under ultraviolet (UV) light, as shown in Fig. S4. Homonuclear compound

(**Tb**) is green and (**Eu**) is red, while heterometallic compounds show different colors, depending on the Tb/Eu ratio.

The excitation spectrum of all complexes presents a shoulder at ca. 280 nm, associated to the UV absorption of the benzoate ligands (Fig. 4a). The Eu f-f transitions $^7F_0 \rightarrow {}^5D_4$ (360 nm), $^7F_0 \rightarrow {}^5G_J$ (385 nm), $^7F_0 \rightarrow {}^5L_6$ (395 nm), $^7F_1 \rightarrow {}^5D_3$ (416 nm) and $^7F_0 \rightarrow {}^5D_2$ (464 nm) are visible for the **Eu** and the heterometallic **TbEu** complexes. The emission spectrum of each compound was measured upon excitation at λ_{exc}=280 nm, to profit from the antenna effect (Fig. 4b). The overall quantum yield via excitation of the ligand Q_{Ln}^{lig} was determined in each case. In addition, for the **Eu** compound the intrinsic quantum yield Q_{Eu}^{Eu} was determined using the method proposed by M. H. V. Werts $et~al.$[58].

Luminescent lifetimes were measured by following the decay of the most intense peak observed in the emission spectrum of each compound ($^5D_4 \rightarrow {}^7F_5$ for Tb^{3+}, $^5D_0 \rightarrow {}^7F_2$ for Eu^{3+}), see Fig. S5. Table 2 summarizes the measured lifetimes τ_{obs}^{Ln} monitored at λ_{mon}, for all the characterized complexes, and the QY values determined from the emission spectra obtained exciting the ligand.

The luminescent properties of the **Tb** analogue had been previously reported by us[56], and are here briefly commented for the sake of comparison with the heterometallic analogues TbEu. The emission spectra (Fig. 4b) show four bands associated to the $^5D_4 \rightarrow$

^7F_J (J = 6, 5, 4, 3) transitions to the ground state multiplet of Tb(III) ion. The main peak at 546 nm corresponds to the $^5D_4 \rightarrow {}^7F_5$. The luminescence lifetime decay, when the Tb^{3+} is excited at this $^5D_4$ level was τ_{obs}^{Tb}= 1.3 ms (see S5), and the quantum yield via excitation of the ligand was sizeable, $Q_{Tb}^{lig} = 61\%$. We note the large QY value despite the difference between the energy of the triplet state (T$_1$) of benzoate[59] (21280 cm^{-1}) and the first excited level of Tb ($^5D_4$) at 20500 cm^{-1} is just of ΔE=780 cm^{-1}, at the limit of the 1500-5500 cm^{-1} range often considered as optimum to avoid energy back transfer in Tb compounds.[60]

The emission spectra of the **Eu** compound when exciting the benzoato ligand (λ_{exc}=280 nm) shows the expected Eu^{3+} transitions $^5D_0 \rightarrow {}^7F_J$ (J = 0-6) and is dominated by the transition $^5D_0 \rightarrow {}^7F_2$ centered at 617.7 nm. The transition $^5D_0 \rightarrow {}^7F_0$ is visible at 579.1 nm, which indicates the absence of an inversion center in the Eu coordination environment. Besides, the ratio between the intensity of the electric-dipole transition $^5D_0 \rightarrow {}^7F_2$ (hypersensitive to the coordination environment) and that of the magnetic dipole transition $^5D_0 \rightarrow {}^7F_1$ is rather large, I = 4.79, which is also in agreement with the relatively low symmetry of the Ln site.[61]
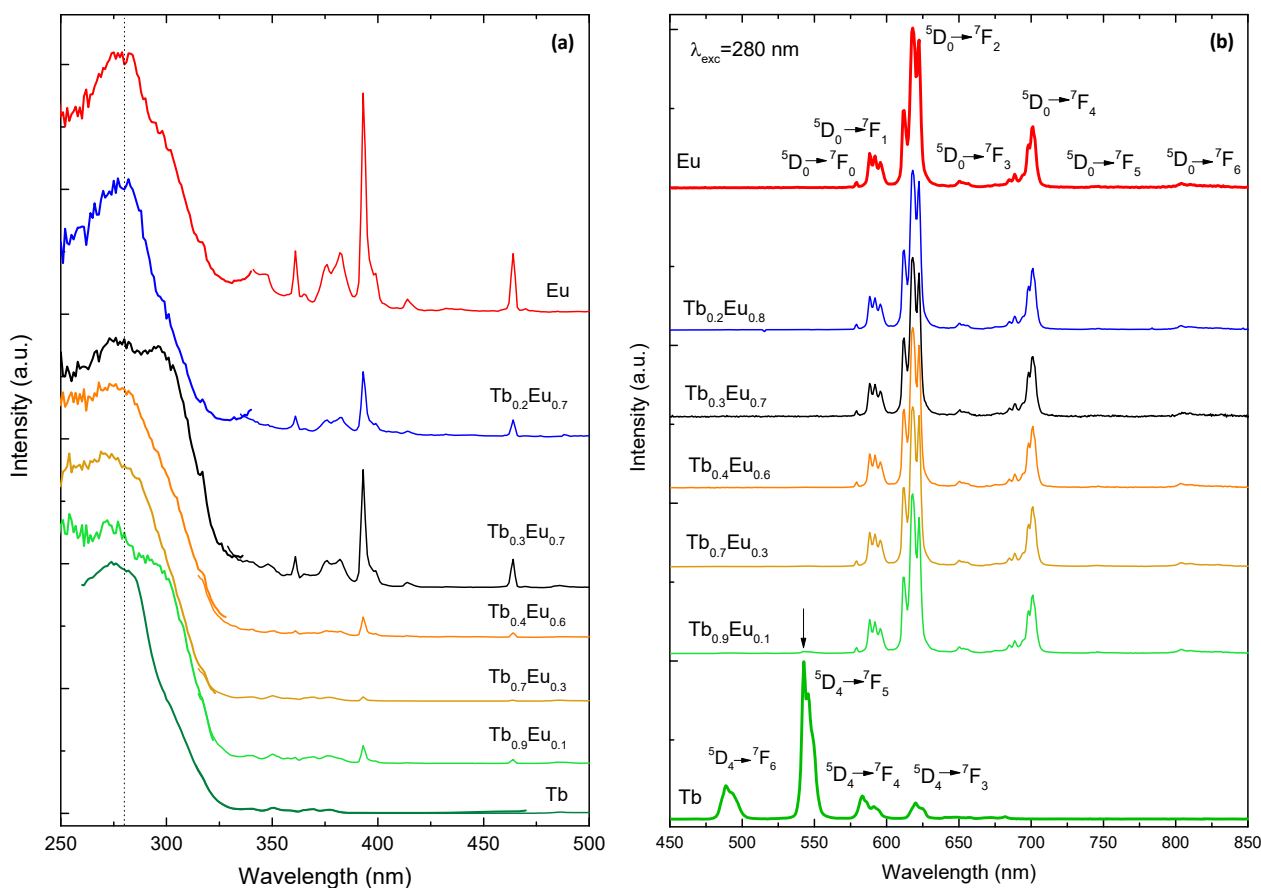
Figure 4 (a) Normalized excitation spectra, monitoring at the indicated wavelengths (thick line λ_{mon1}, thin line λ_{mon2}) **Tb** (λ_{mon1} = 490 nm, λ_{mon2} = 544 nm), **Tb$_{0.9}$Eu$_{0.1}$**, **Tb$_{0.7}$Eu$_{0.3}$**, **Tb$_{0.3}$Eu$_{0.7}$**, **Eu**, (λ_{mon1} = 700 nm, λ_{mon2} = 620 nm), **Tb$_{0.4}$Eu$_{0.6}$**, **Tb$_{0.2}$Eu$_{0.8}$** (λ_{mon1} = 700 nm, λ_{mon2} = 590 nm), and (b) normalized emission spectra, exciting the ligand at λ_{exc}=280 nm. The arrow signals the position of Tb^{3+} main peak that starts to be visible in **Tb$_{0.8}$Eu$_{0.2}$**.

ARTICLE
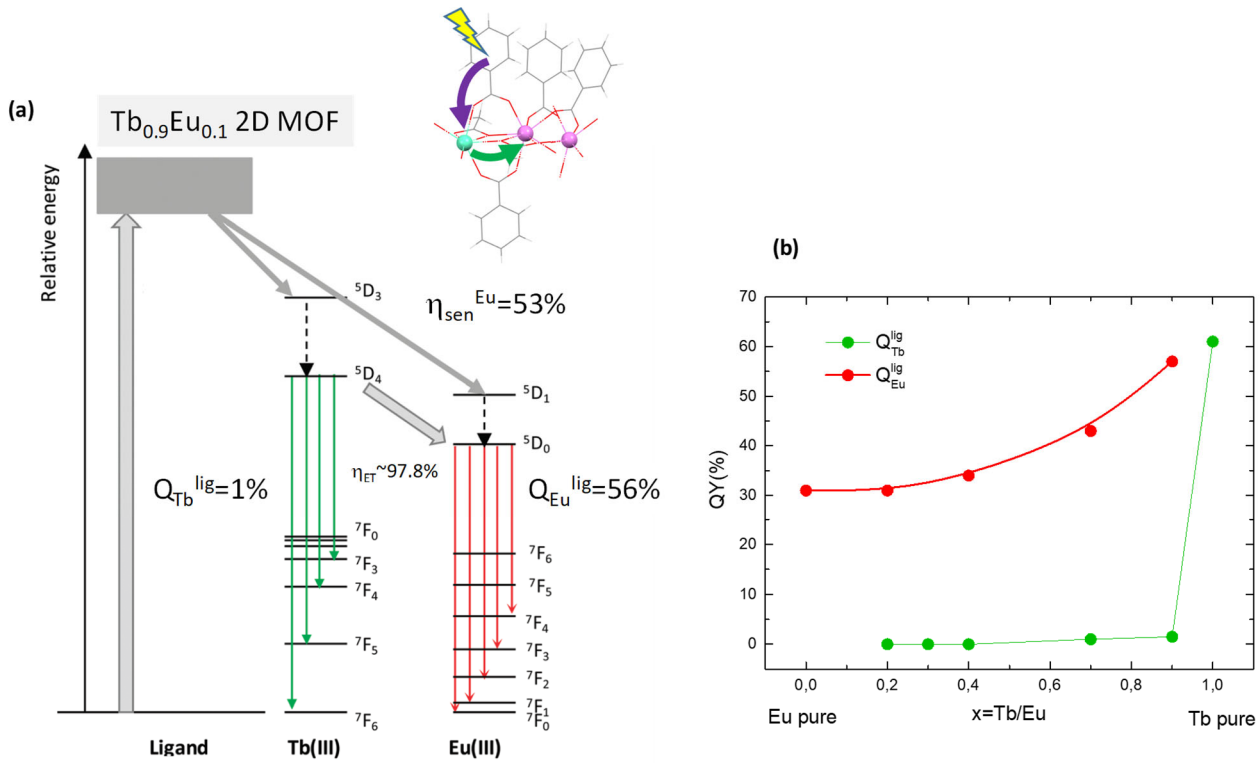
Figure 5. (a) Energy level scheme and proposed ET mechanisms for **Tb$_{0.9}$Eu$_{0.1}$** 2D MOF complex; (b) total quantum yield upon excitation at λ_{exc} = 280 nm for pure and heterometallic Tb$_x$Eu$_{1-x}$ compounds as a function of the x=Tb/Eu ratio.

The luminescence relaxation time decay of the 617 nm band, when Eu^{3+} is excited through the ligand (280 nm), was τ_{obs}^{Eu} = 1.471 ms. A total quantum yield of Q_{Eu}^{lig} = 31% was obtained via ligand-mediated excitation. The energy separation between the benzoate antenna triplet state T$_1$ and the excited state for Eu (^{5}D$_0$) at 17500 cm^{-1} is ΔE=3780 cm^{-1}, within the 1000 to 5000 cm^{-1} optimal range to obtain sizeable QYs in Eu compounds, as found by different authors.[62–64]

The efficiency of the ligand-to-lanthanoid energy transfer is defined as:[65]

$$\eta_{sens}^{Ln} = \frac{Q_{Ln}^{ligand}}{Q_{Ln}^{Ln}}, \qquad [2]$$

where Q_{Ln}^{Ln} is the intrinsic quantum yield of the lanthanoid upon direct excitation, which can be determined as the ratio between the observed and radiative lifetimes:

$$Q_{Ln}^{Ln} = \frac{\tau_{obs}^{Ln}}{\tau_{rad}^{Ln}}, \qquad [3]$$

For the **Eu** compound, it is possible to determine the intrinsic quantum yield Q_{Eu}^{Eu}, since the radiative lifetime can be estimated as:[58]

$$\frac{1}{\tau_{rad}^{Eu}} = A_{MD,0} n^3 \left(\frac{I_{tot}}{I_{MD}} \right), \qquad [4]$$

where the $A_{MD,0}$ = 14.65 s^{-1} constant is the spontaneous emission probability of the magnetic dipole ^{5}D$_0$ → ^{7}F$_1$, n is the refractive index, I_{tot} is the integrated emission of the ^{5}D$_0$ → ^{7}F$_J$ (J = 0–6) transitions, and I_{MD} is the integrated emission of the magnetic dipole ^{5}D$_0$ → ^{7}F$_1$ transition. The refractive index was approximated as n ≈ 1.5.[66,67] Using this procedure we deduced an intrinsic yield of Q_{Eu}^{Eu} = 58.1%. Considering the measured total quantum yield via ligand-ediated excitation (Table 2), the sensitization factor was found to be $\eta_{sens}^{Eu} \approx 53\%$. This value indicates that benzoates are efficient ligands for the sensitization of Eu ion in this 2D MOF.[64]

The emission spectra of the heterometallic **TbEu** complexes excited at λ_{exc} = 280 nm via the ligand ligand show essentially the characteristic bands of Eu^{3+} (Fig. 4b). Only for the complex with the largest Tb/Eu ratio, **Tb$_{0.9}$Eu$_{0.1}$**, the Tb^{3+} emission bands could be seen

superimposed to the Eu^{3+} transitions (Fig. S7). In this case the quantum yield

Table 2 Photoluminescent data determined for TbEu 2D-MOF complexes, by exciting the ligand at λ_{exc} =280 nm.

Complex	Q_{Eu}^{lig}(%)	Q_{Tb}^{lig}(%)	τ_{obs}^{Eu}(ms)	τ_{obs}^{Tb}(ms)
Eu	31	-	1.471(4)	-
Tb$_{0.2}$Eu$_{0.8}$	31	0	1.597(4)	-
Tb$_{0.3}$Eu$_{0.7}$	-	-	1.468(3)	-
Tb$_{0.4}$Eu$_{0.6}$	34	0	1.609(4)	-
Tb$_{0.7}$Eu$_{0.3}$	43	0	1.735(9)	-
Tb$_{0.9}$Eu$_{0.1}$ (RT)	56	1	1.678(4)	0.82(5), 0.029(1)
Tb$_{0.9}$Eu$_{0.1}$ (LNT)			1.212	0.080(1) + background
Tb	-	61	-	1.31(4)
Tb (exf. sol.)	-	69	-	1.29(1)

contributions for the two ions could be estimated from the total quantum yield, considering the relative intensities of the Tb^{3+} and the Eu^{3+} peaks, yielding Q_{Eu}^{lig} = 56% and Q_{Tb}^{lig} = 1%. The luminescent lifetimes τ_{obs}^{Eu} and τ_{obs}^{Tb} were monitored by following the decay of the Eu^{3+} main peak (620 nm) and Tb^{3+} peak (544 nm), see Fig. S5. Terbium emission decay was fit by a logarithmic decay function with two very short relaxation times (see Table 2). The efficiency of energy transfer (ET) in the mixed compounds can be quantified as:

$$\eta_{ET} = 1 - \frac{\tau_{obs}}{\tau_0}, \qquad [5]$$

where $\tau_{obs} = \tau_{obs}^{Tb}$[TbEu] and $\tau_0 = \tau_{obs}^{Tb}$[Tb]. For **Tb$_{0.83}$Eu$_{0.17}$**, the energy transfer (calculated with τ_{obs}^{Tb}[Tb] $= \tau_1 = 0.029\ ms$, the shortest lifetime of the biexponential decay determining the ET, and τ_{obs}^{Tb}[Tb] $= 1.31\ ms$), is very large, $\eta_{ET} = 97.8$ %. In the rest of mixed compounds the Tb^{3+} transitions are not observed, indicating ET is practically complete, $\eta_{ET} \approx 100$ %. The energy transfer diagram suggested for the **TbEu** 2D MOFs is schematized in Fig. 5a.

Figure 5b shows the dependence of the total quantum yield (Q_{Ln}^{lig}) for the Tb$_x$Eu$_{1-x}$ compounds as a function of the x=Tb/Eu ratio. It shows an increase of Europium quantum yield (Q_{Eu}^{lig}) with increasing the Tb/Eu fraction thanks to Tb sensitization.

The thermometric properties of **Tb$_{0.9}$Eu$_{0.1}$** in the solid state were evaluated by measuring the emission spectra at room temperature (RT) and liquid nitrogen temperature (LNT). As shown in Figure 6, the intensities of Tb^{3+} bands increase relative to those of Eu^{3+} upon cooling from 300 K to 77 K. It is observed that the luminescent lifetime of the main Eu^{3+} peak (τ_{obs}^{Eu}) decreases (S6 and Table 2).

We calculated the thermometric parameter $\Delta = I_{Tb}/I_{Eu}$, defined as the ratio between the integrated areas of the Tb^{3+} $^5D_4 \rightarrow ^7F_5$ (538-556 nm), I_{Tb}, and Eu^{3+} $^5D_0 \rightarrow ^7F_2$ (584-602 nm), I_{Eu}, emissions.[68] The thermometric parameter changed from Δ(LNT)=0.333 to Δ(RT)=0.142, i.e. a factor of 2.4, showing the potential of these compounds as luminescent thermometers.
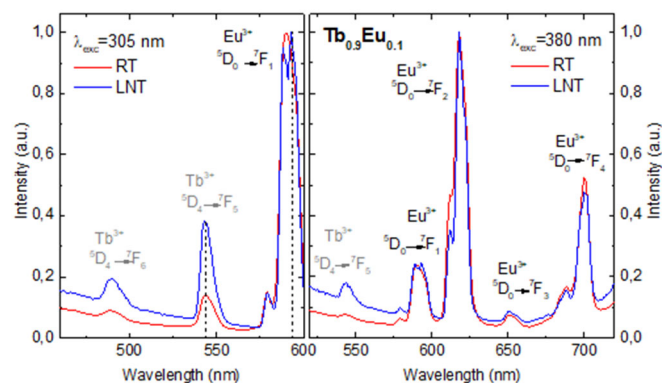
Figure 6. Emission spectra of the **Tb$_{0.9}$Eu$_{0.1}$** compound at room temperature (RT, red trace) and at liquid nitrogen temperature (LNT, blue trace) at the indicated excitation wavelength.

Luminescence of exfoliated solutions. All the 2D materials prepared in this work can be exfoliated in solution by sonication. In particular, we discuss here the luminescent results obtained for exfoliations prepared from the homometallic compounds **Tb** and **Eu**.

Figure 7a shows the green emission observed under UV light for a solution containing exfoliated nanosheets of Tb, prepared using the exfoliation procedure (1) detailed in the experimental section. The emission spectrum shows the expected transitions for Tb^{3+}. The emission lifetime was long, similar to that measured for the bulk, τ_{obs}^{Tb}=1.29 ms, and the quantum yield was enhanced, reaching a remarkable high value of Q_{Tb}^{lig}=69% (Table 2). We had already shown that flakes of Tb 2D MOF deposited on a silicon wafer by spin-coating remain luminescent.[56]
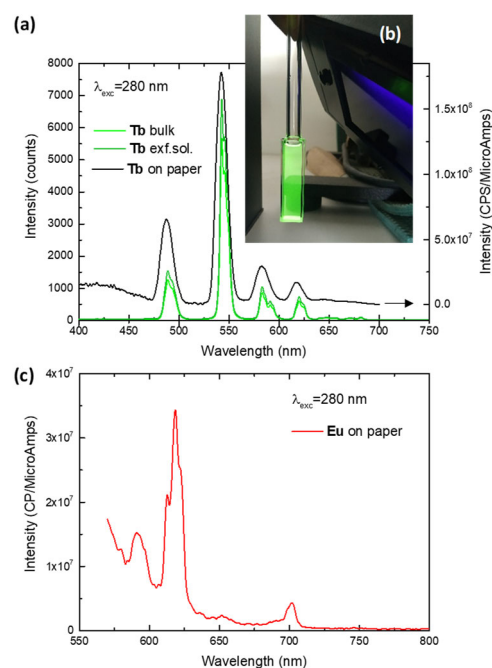

Figure 7 (a) Emission spectra of the **Tb** compound in solid, the exfoliated solution and exfoliations on paper (after subtraction of paper emission), upon excitation at 280 nm; (b) green emission of the isopropanol solution with exfoliations under UV light; (c) Emission spectra of **Eu** exfoliations on paper.

The prepared solutions of exfoliated Ln-2D MOFs may be used as luminescent inks for several applications, e.g. anticounterfeiting. To proof the concept, we prepared prints of **Tb** and **Eu** 2D MOF inks on paper. For the **Tb** print, we used an exfoliated solution prepared following procedure (3). 10 drops of a 50 μL micropipette were poured into a filter paper one by one. The Tb^{3+} transitions were clearly observed in the fluorimeter, as shown in Fig. 7a. For the **Eu** print, the exfoliation procedure (3) was used to increase the concentration of nanosheets in solution to obtain a visible luminescent signal, and 10 drops of 1 μL were deposited on paper. As shown in Fig. 7b, the obtained print exhibited the expected Eu^{3+} transitions.

5. Magnetic results

Dc magnetometry. The magnetic characterization was focused on the TbEu compounds, including results of homonuclear **Eu** and **Tb** counterparts as a reference.
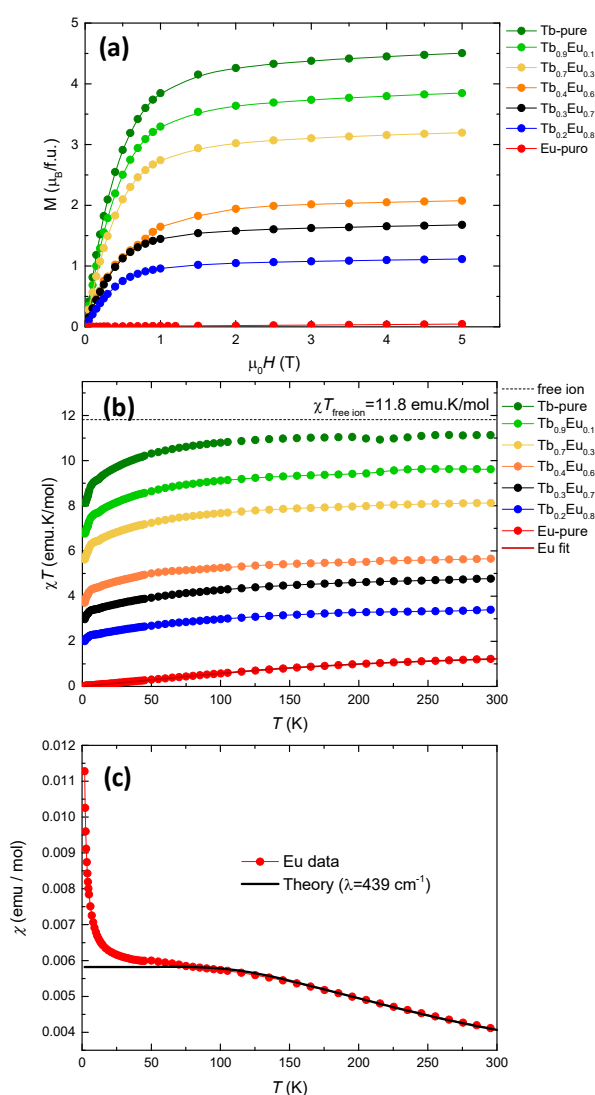
Figure 8 Static magnetic properties for **Tb$_{0.9}$Eu$_{0.1}$, Tb$_{0.7}$Eu$_{0.3}$, Tb$_{0.4}$Eu$_{0.6}$, Tb$_{0.3}$Eu$_{0.7}$, Tb$_{0.2}$Eu$_{0.8}$** and **Eu** (a) field-dependence of the magnetization per formula unit, $M(H)$, measured at T=1.8 K, and (b) field-dependence of the susceptibility times the temperature at 1 kOe; (c) susceptibility $vs.$ temperature data for **Eu** and fit to Eq. [6].

Fig. 8a shows the magnetic-field dependence of the magnetization $M(H)$ at T = 1.8 K measured for **Tb** compound and heterometallic compounds with decreasing Tb/Eu ratio (**Tb$_{0.9}$Eu$_{0.1}$, Tb$_{0.7}$Eu$_{0.3}$, Tb$_{0.4}$Eu$_{0.6}$, Tb$_{0.3}$Eu$_{0.7}$, Tb$_{0.2}$Eu$_{0.8}$**).

The saturation magnetization at 50 kOe for the **Tb** compound approaches the expected values of M_{sat}= 4.5 μ$_B$ at very low temperatures (Tb^{3+}, g_z^* = 18, S* = 1/2), and it decreases in the mixed compounds in correlation with the diminished amount of Tb. The dc magnetic susceptibilities of the same compounds under 1 kOe field from 1.8 to 300 K are shown in Fig. 8b.

For the **Tb** compound, the room temperature χT product reaches a value of 11.1 emuKmol^{-1} consistent with the expected theoretical value at high temperatures, $\chi T_{free-ion}$ = $g_J^2 J(J + 1)/8$=11.8 emuKmol^{-1} for Tb^{3+}($^7F_6$, g_J = 3/2).

For TbEu compounds, the χT_{300K} value reaches the expected value considering the proportion of Tb/Eu in each formula unit.

For **Eu** compound, the temperature dependence of the susceptibility, $\chi(T)$ at 1 kOe between 1.8-300 K, is plotted in Fig. 8c. The $\chi(T)$ curve shows that as the temperature is decreased from room temperature, χ increases smoothly and tends to a plateau, increasing at very low temperatures most likely due to some spurious magnetic impurities.

Similar features have been earlier reported for Eu(III)-complexes.[69,70] In Eu(III) the ^7F ground term is split by the spin-orbit coupling into seven states, ^7F_J, with J taking integer values from 0 to 6, and the energies of the states are E(J) = λJ(J+1)/2, where λ is the spin-orbit constant and the energy of the $^7F_0$ ground state is taken at the origin. Given that λ is relatively small, the crystal field (CF) components of the first and second excited states can be thermally populated, giving rise to a paramagnetic response to the application of an external magnetic field. The $\chi(T)$ data could be well fitted with the theoretical isotropic equilibrium magnetic susceptibility as a function of temperature at zero field within the Van Vleck approximation:[69]

$$\chi = \frac{\sum_{J=0}^{6}(2J+1)\chi(J)\exp\left[-\lambda J(J+1)/2k_BT\right]}{\sum_{J=0}^{6}(2J+1)\exp\left[-\lambda J(J+1)/2k_BT\right]}, \quad [6]$$

with a spin-orbital parameter of λ = 439 K = 305.12 cm^{-1}. This value is in good agreement with that obtained from the luminescence, given by the energy splitting between the $^7F_0$ and the center of gravity of the $^7F_1$ term, which yielded λ = 311.6 cm^{-1}.

Finally, we investigated the magnetic properties of the exfoliated 2D MOFs in solution. Fig.9 shows the $M(H)$ and $\chi T(T)$ curves measured for a frozen solution of exfoliated **Tb**, compared with results obtained for the bulk. For the exfoliated solution, the estimated diamagnetic contribution from isopropanol, m_{diag} = -1.1 10^{-7} emu, was subtracted.

The total amount of nanosheets is unknown, therefore the figures display the values for the measured moment, corrected from the diamagnetic contribution of the solvent. Different scales for the frozen solution and the bulk are used for comparison. The $m(H)$ of the exfoliated solution lies below that of the bulk (Fig. 9a), and the $\chi T(T)$ decreases steeply with decreasing the temperature (Fig. 9b). Both results indicate that antiferromagnetic interactions are more dominant in the exfoliated samples. A plausible explanation is that the exfoliation of the material in 2D flakes is removing the magnetic interaction between nanosheets, giving more weight to the in-plane AF interactions.
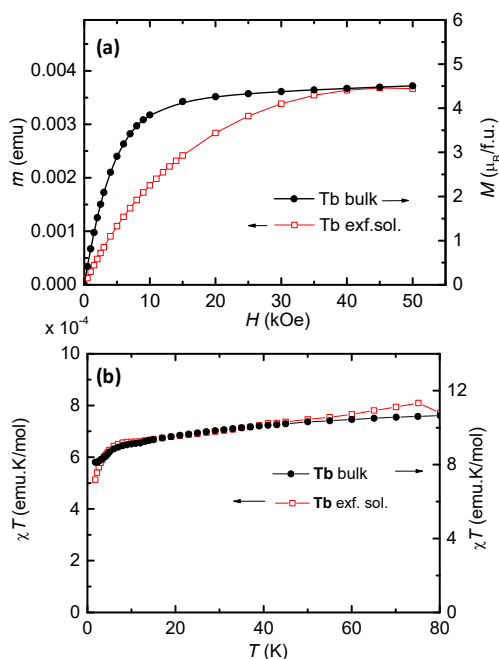
Figure 9 Static magnetic properties for a frozen solution of **Tb** nanosheets in isopropanol, compared to results for **Tb** in bulk. (a) Magnetization as a function of the field at T=1.8 K; (b) temperature-dependence of the susceptibility times the temperature at 1 kOe.

Dynamic results. Ac magnetic susceptibility measurements as a function of frequency (f = 0.1-10^4 Hz) were performed to study the dynamics of magnetic relaxation of the heterometallic Tb_xEu_{1-x} species and the Tb counterpart (Fig. 10 and Fig. S8). None of the compounds showed out-of-phase (χ'') signal in the absence of a dc magnetic field below 8 K, indicating a significant quantum tunneling of the magnetization (QTM) channel preventing slow spin relaxation. $\chi''(f, H)$ measurements at constant T = 2 K under fields from 0 to 20 kOe were performed to investigate the effect of field on magnetic relaxation (Figs. 10b,d,f). $\chi''(f, T)$ measurements were recorded at the optimum field (Figs. 10a,c,e). For the Tb compound, the $\chi''(f, T, H)$ data show a clear maximum at low frequencies (LF) and a shoulder at higher frequencies (HF). In the case of the heterometallic Tb_xEu_{1-x} compounds, the LF peak shifts to higher frequencies in correlation with the decrease in the fraction of Tb ions, whereas the HF merges into a broad peak and is no more discernible.

The relaxation time of the two paths as a function of the inverse of the temperature and the field, $\tau_{LF}(1/T, H)$ and $\tau_{HF}(1/T, H)$, were determined from the $\chi''(f, H, T)$ peak positions (Figs. 10g, h). The temperature and field dependencies of the LF process observed in all the compounds is characteristic of a direct, slow relaxation mechanism affected by bottleneck effect (BE). The BE takes place when the energy of the lattice modes generated by the relaxing spins cannot be released into the thermal bath at sufficiently high rate.[71,72] The influence of the BE was demonstrated by making relaxation experiments at different conditions on **Tb** compound. As shown in Fig. S9, the main relaxation peak was shifted by an order of magnitude to larger frequencies by increasing the chamber pressure. The process was fully reversible.

Figs. 10g, h show that the relaxation times tend to decrease and multiple χ'' peaks tend to appear as the Tb/Eu ratio decreases. This effect has been earlier described in heterometallic [TbEu] furoate

compounds.[73] In a direct process affected by BE the relaxation time $\tau_{d,BE}$ depends on the intrinsic spin relaxation time (τ_{SL}), the lattice-bath relaxation time (τ_{LB}) and the magnetic-to-lattice heat capacity ratio as: $\tau_{d,BE}=\tau_{SL}+(C_m/C_L).\tau_{LB}$. In the mixed compounds, the decrease in the C_m/C_L contribution owed to the dilution of magnetic ions causes the reduction of $\tau_{d,BE}$. The occurrence of multiple χ'' peaks associated to a single relaxation through the bath has been also previously reported.[74,75]

6. Conclusions

We have applied a simple microwave assisted synthesis to Van der Waals 2D MOFs to prepare heterometallic systems of general formula $[Tb_xEu_{1-x}(MeCOO)(PhCOO)_2]$, with variable Tb/Eu ratios, which are isostructural to the Dy and Tb counterparts previously described. The method can be extended to the synthesis of other combinations of Ln/Ln' heterometallic 2D MOFs.

Photoluminescent emission in the visible range was observed for Eu and Tb 2D MOF pure compounds via ligand-mediated excitation, showing benzoates act as good antenna ligands. Efficient energy transfer from Tb→Eu was observed in the heterometallic compounds, which interestingly, showed temperature-dependent luminescent and may be potentially ised as thermometers. The Van der Waals nature of these systems allows easy exfoliation into flakes and single nanosheets in i-PrOH. Luminescent inks containing nanosheets of 2D MOFs exfoliated in solution could be prepared. Luminescence of the iPrOH suspension of the **Tb** and **Eu** MOFs stamped on paper were successfully observed, as a proof of concept of the use of these materials for anticounterfeiting applications.

The magnetic properties of Tb_xEu_{1-x} compounds with varying ratio x=Tb/Eu were analyzed in detail. The static magnetization behavior reflects the presence of Tb-Eu ions in a ratio in consistent with ICP results. Frequency-dependent ac susceptibility results show the occurrence of slow magnetic relaxation in TbEu compounds through direct relaxation mechanisms, affected by bottleneck effects. A slowing down of the relaxation time is observed as the Tb/Eu ratio increases.

In summary, we have presented an effective approach to develop heterometallic multifunctional TbEu 2D MOFs that combine SMM properties with luminescence. The facile exfoliation of Ln-2D MOFs into stable nanosheets is very promising for further applications of these materials in smart inks, for the deposition of flakes or grafting of 2D MOFs onto different surfaces, or the combination of this material with inorganic 2D materials forming multilayer heterostructures.

Acknowledgements

ARTICLE
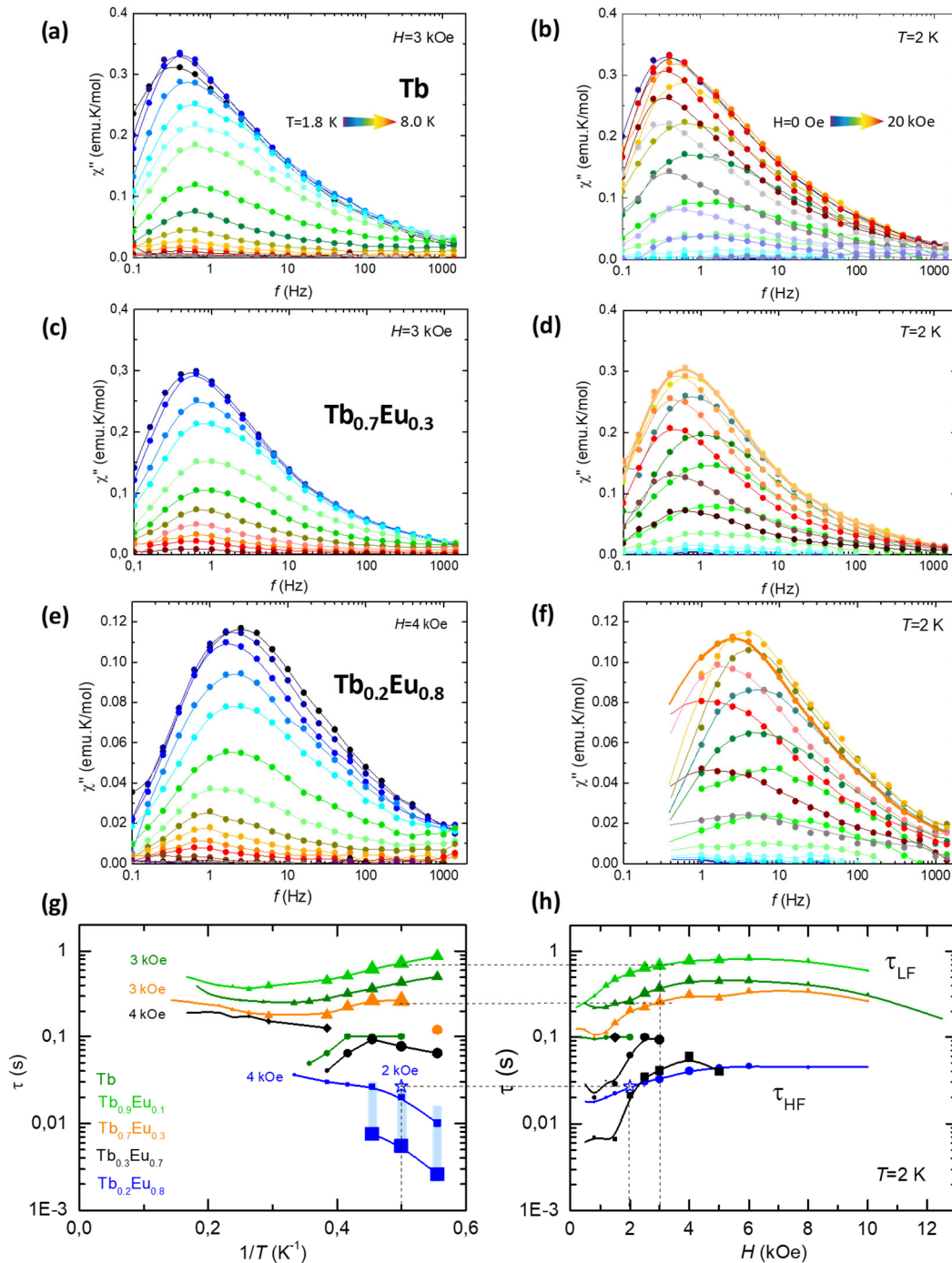
Figure 10 Ac susceptibility results. (Left) $\chi''(f, T)$ at constant magnetic field H, and (Right) $c''(f, H)$ at constant T=2 K for (a)-(b) **Tb** compound, and mixed compounds (c)-(d) **Tb$_{0.7}$Eu$_{0.3}$** and (e) −(f) **Tb$_{0.2}$Eu$_{0.8}$**; (g) Relaxation time *vs.* inverse of the temperature for pure and mixed compounds, and (h) relaxation time as a function of the applied field, at T=2.0 K. The relaxation times for the two observed processes are denoted τ_{LF} and τ_{HF}.

ARTICLE

References

1. S. V Eliseeva and J.-C. G. Bünzli, *Chem. Soc. Rev.*, 2010, **39**, 189–227.
2. A. Amoroso and S. Pope, *Chem. Soc. Rev.*, 2015, **44**, 4723–4742.
3. M. Evangelisti, *Mol. MAGNETS Phys. Appl.*, 2014, 365–387.
4. M. Falsaperna and P. Saines, *Dalt. Trans.*, 2022, **51**, 3394–3410.
5. K. Jinnai, R. Kabe and C. Adachi, *Chem. Commun.*, 2017, **53**, 5457–5460.
6. J. Kido and Y. Okamoto, *Chem. Rev.*, 2002, **102**, pp.2357-2368.
7. L. Sorace and D. Gatteschi, eds. R. Layfield and M. Murugesu, Wiley-VCH., 2015.
8. E. Bartolomé, A. Arauzo, J. Luzón, J. Bartolomé and F. Bartolomé, in *Handbook of Magnetic Materials*, 2017, vol. 26, pp. 1–289.
9. J. Zhou, Q. Liu, W. Feng, Y. Sun and F. Li, *Chem. Rev.*, 2015, **115**, 395–465.
10. S. Freslon, Y. Luo, C. Daiguebonne, G. Calvez, K. Bernot and O. Guillou, *Inorg. Chem.*, 2016, **55**, 794–802.
11. E. Bartolomé, J. Bartolomé, A. Arauzo, J. Luzón, R. Cases, S. Fuertes, V. Sicilia, A. I. Sánchez-Cano, J. Aporta, S. Melnic, D. Prodius and S. Shova, *J. Mater. Chem. C*, 2018, **6**, 5286–5299.
12. O. Guillou, C. Daiguebonne, G. Calvez and K. Bernot, *Acc. Chem. Res.*, 2016, **49**, 844–856.
13. I. Mamedov, T. Parac-Vogt, N. Logothetis and G. Angelovski, *Dalt. Trans.*, 2010, **39**, 5721–5727.
14. A. Abdallah, S. Freslon, X. Fan, A. Rojo, C. Daiguebonne, Y. Suffren, K. Bernot, G. Calvez, T. Roisnel and O. Guillou, *Inorg. Chem.*, 2019, **58**, 462–475.
15. X. Rao, T. Song, J. Gao, Y. Cui, Y. Yang, C. Wu, B. Chen and G. Qian, *J. Am. Chem. Soc.*, 2013, **135**, 15559–15564.
16. D. Aguila, O. Roubeau and G. Aromi, *Dalt. Trans.*, 2021, **50**, 12045–12057.
17. G. Aromí, D. Aguilà, P. Gamez, F. Luis and O. Roubeau, *Chem. Soc. Rev.*, 2012, **41**, 537–546.
18. D. Aguilà, L. A. Barrios, V. Velasco, O. Roubeau, A. Repollés, P. J. Alonso, J. Sesé, S. J. Teat, F. Luis and G. Aromí, *J. Am. Chem. Soc.*, 2014, **136**, 14215–14222.
19. J. Le Roy, J. Cremers, I. Thomlinson, M. Slota, W. Myers, P. Horton, S. Coles, H. Anderson and L. Bogani, *Chem. Sci.*, 2018, **9**, 8474–8481.
20. V. Velasco, L. Barrios, M. Schutze, O. Roubeau, F. Luis, S. Teati, D. Aguila and G. Aromi, *Chem. Eur. J.*, 2019, **25**, 15228–15232.
21. E. Macaluso, M. Rubin, D. Aguila, A. Chiesa, L. Barrios, J. Martinez, P. Alonso, O. Roubeau, F. Luis, G. Aromi and S. Carretta, *Chem. Sci.*, 2020, **11**, 10337–10343.
22. J.-C. G. Bünzli and C. Piguet, *Chem. Soc. Rev.*, 2005, **34**, 1048–1077.
23. B. Sieklucka and D. Pinkowicz, Eds., *Molecular Magnetic Materials*, Wiley-VCH Verlag GmbH, Weinheim, Germany, 2017.
24. S. V. Eliseeva and J.-C. G. Bünzli, *Chem. Soc. Rev.*, 2010, **39**, 189–227.
25. D. Prodius and A.-V. Mudring, *Coord. Chem. Rev.*, 2018, **363**, 1–16.
26. R. Sessoli and A. K. Powell, *Coord. Chem. Rev.*, 2009, **253**, 2328–2341.
27. R. A. Layfield and M. Murugesu, *Lanthanides and Actinides in Molecular Magnetism*, Wiley-VCH Verlag&Co. KGaA, 2015.
28. F.-S. Guo, B. M. Day, Y.-C. Chen, M.-L. Tong, A. Mansikkamäki and R. A. Layfield, *Science*, 2018, **364**, 1400–1403.
29. J.-P. Costes, F. Dahan and F. Nicodème, *Inorg. Chem.*, 2003, **42**, 6556–6563.
30. D. Lewis, P. Glover, M. Solomons and Z. Pikramenou, *J. Am. Chem. Soc.*, **133**, 1033–1043.
31. P. Zhu, N. Pan, R. Li, J. Dou, Y. Zhang, D. Y. Y. Cheng, D. Wang, D. K. P. Ng and J. Jiang, *Chem. Eur. J.*, 2005, **11**, 1425–1432.
32. S. Faulkner and S. J. A. Pope, *J. Am. Chem. Soc.*, 2003, **125**, 10526–10527.
33. L. Natrajan, A. Villaraza, A. J. L., A. Kenwright and S. Faulkner, *Chem. Commun.*, 2009, 6020–6022.
34. M. Placidi, A. Villaraza, L. Natrajan, D. Sykes, A. Kenwright and S. Faulkner, *J. Am. Chem. Soc.*, 2009, **131**, 9916–9917.
35. N. Andre, T. Jensen, R. Scopelliti, D. Imbert, M. Elhabiri, G. Hopfgartner, C. Piguet and J. Bunzli, *Inorg. Chem.*, 2004, **43**, 515–529.
36. N. Andre, R. Scopelliti, G. Hopfgartner, C. Piguet and J. Bunzli, *Chem. Commun.*, 2002, 214–215.
37. S. Floquet, M. Borkovec, G. Bernardinelli, A. Pinto, L. Leuthold, G. Hopfgartner, D. Imbert, J. Bunzli and C. Piguet, *Chem. Eur. J.*, 2004, **10**, 1091–1105.
38. Y. Lan, S. Klyatskaya, M. Ruben, O. Fuhr, W. Wernsdorfer, D. A. Candini, V. Corradini, A. L. Rizzini, U. del Pennino, F. Troiani, L. ¨c Joly, D. Klar, H. Wendeh and M. Affrontef, *J. Mater. Chem. C*, 2015, **3**, 9794–9801.
39. R. Sato, K. Suzuki, M. Sugawa and N. Mizuno, *Chem. Eur. J.*, 2013, **19**, 12982–12990.
40. A. Topor, D. Avram, R. Dascalu, C. Maxim, C. Tiseanu and M. Andruh, *Dalt. Trans.*, 2021, **50**, 9881–9890.
41. M. Rodrigues, J. Dutra, L. Nunes, G. de Sa, W. de Azevedo, P. Silva, F. Paz, R. Freire and S. Junior, *J. Phys. Chem. C*, 2012, **116**, 19951–19957.
42. X. Peng, Q. Liu, H. Wang and Y. Wang, *Dye. Pigment.*, 2019, **162**, 405–411.
43. D. Zhao, D. Yue, L. Zhang, K. Jiang and G. Qian, *Inorg. Chem.*, 2018, **57**, 12596–12602.
44. Y. Yang, H. Huang, Y. Wang, F. Qiu, Y. Feng, X. Song, G. Xiaoliang Tang, Zhang and W. Liu, *Dalt. Trans.*, 2018, **47**, 13384–13390.
45. E. Coronado, *Nat. Rev. Mater.*, 2020, **5**, 87–104.
46. M. Zhao, Y. Huang, Y. Peng, Z. Huang, Q. Ma and H. Zhang, *Chem. Soc. Rev.*, 2018, **47**, 6267–6295.
47. D. D. Yin, Q. Chen, Y. S. Meng, H. L. Sun, Y. Q. Zhang and S. Gao, *Chem. Sci.*, 2015, **6**, 3095–3101.
48. P. Miró, M. Audiffred and T. Heine, *Chem. Soc. Rev.*, 2014, **43**, 6537–6554.
49. B. Wang, J. Jin, B. Ding, X. Han, A. Han and J. Liu, *Front. Mater.*, 2020, **7**, 37.
50. G. Ding, Y. Wang, G. Zhang, K. Zhou, K. Zeng, Z. Li, Y. Zhou, C. Zhang, X. Chen and S.-T. Han, *Adv. Funct. Mater.*, 2019, **29**,

1806637.

51 D. J. Ashworth and J. A. Foster, *J. Mater. Chem. A*, 2018, **6**, 16292–16307.

52 B. Pepi, N. Contreras-Pereda, S. Suárez-García, P. Hayatia, S. Benmansourb, R. Pascal, A. Morsalid and D. Ruiz-Molina, *Ultrason. Sonochem.*, 2021, **72**, 105425.

53 L. León-Alcaide, J. López-Cabrelles, G. M. Espallargas and E. Coronado, *Chem. Commun.*, 2020, **56**, 7657–7660.

54 X. Lu, Y. Tang, G. Yang and Y.-Y. Wang, *J. Mater. Chem. C*, , DOI:10.1039/d2tc04978c.

55 J. González, P. Sevilla, G. Gabarró-Riera, J. Jover, J. Echeverría, S. Fuertes, A. Arauzo, E. Bartolomé and E. C. Sañudo, *Angewandte*, 2021, **60**, 12001–12006.

56 E. Bartolomé, A. Arauzo, S. Herce, A. Palau, N. Mestres, S. Fuertes, P. Sevilla, N. S. Settineri, L. Navarro-Spreafico, J. González and E. C. Sañudo, *Molecules*, 2021, **26(18)**, 5503.

57 J. Costes and F. Nicodeme, *Chem. Eur. J.*, **8**, 3442–3447.

58 M. H. V. Werts, R. T. F. Jukes and J. W. Verhoeven, *Phys. Chem. Chem. Phys.*, 2002, **4**, 1542–1548.

59 V. I. Tsaryuk, K. P. Zhuravlev, V. F. Zolin, V. A. Kudryashova, J. Legendziewicz and R. Szostak, *J. Appl. Spectrosc.*, 2007, **74**, 52–59.

60 M. Latva, H. Takalo, V.-M. Mukkala, C. Matachescu, J. C. Rodríguez-Ubis and J. Kankare, *J. Lumin.*, 1997, **75**, 149–169.

61 K. Binnemans, *Coord. Chem. Rev.*, 2015, **295**, 1–45.

62 K. Binnemans, *Coord. Chem. Rev.*, 2015, **295**, 1–45.

63 Y. Ma and Y. Wang, *Coord. Chem. Rev.*, 2010, **254**, 972–990.

64 A. Arauzo, L. Gasque, S. Fuertes, C. Tenorio, S. Bernès and E. Bartolomé, *Dalt. Trans.*, 2020, **49**, 13671–13684.

65 J.-C. G. Bünzli and S. V. Eliseeva, in *Lanthanide Luminescence: Photophysical, Analyticaland Biological Aspects*, eds. P. Hänninen and H. Härma, Springer-Verlag, Berlin Heidelberg, 2010.

66 N. M. Shavalev, S. V. Eliseeva, R. Scopelliti and J.-C. G. Bünzli, *Inorg. Chem.*, 2020, **54**, 9166–9173.

67 A. Aebisher, F. Gumy and J.-C. G. Bünzli, *Phys. Chem. Chem. Phys.*, 2009, **11**, 1346–1353.

68 C. D. S. Brites, P. P. Lima, N. J. O. Silva, A. Millán, V. S. Amaral, F. Palacio and L. D. Carlos, *Nanoscale*, 2012, **4**, 4799–4829.

69 M. Andruh and P. Porchers, *Luminescence*, 1993, 1616–1622.

70 A. Arauzo, A. Lazarescu, S. Shova, E. Bartolomé, R. Cases, J. Luzón, J. Bartolomé and C. Turta, *Dalton Trans.*, 2014, **43**, 12342–12356.

71 Q. Li, T. Li and J. Wu, *J.Phys. Chem. B*, 2001, **105**, 12293–12296.

72 R. R. Schenker, M. N. Leuenberger, G. Chaboussant, D. Loss and H. U. Güdel, *Phys. Rev. B Condens. Matter*, 2005, **72**, 184403–184413.

73 E. Bartolomé, J. Bartolomé, A. Arauzo, J. Luzón, R. Cases, S. Fuertes, V. Sicilia, A. I. Sánchez-Cano, J. Aporta, S. Melnic, D. Prodius and S. Shova, *J. Mat. Chem. C*, 2018, **6**, 5286–5299.

74 G. J. Gerritsma, J. Flokstra, G. A. Hartemink, J. J. M. Scholten, A. J. W. A. Vermeulen and L. C. van der Marel, *Phys. B&C*, 1978, **95**, 173–182.

75 J. Flokstra, G. J. Gerritsma, G. A. Hartemink and L. C. van der Marel, *Physica*, 1974, **77**, 99–120.